Improved Design of an Advanced Ice Giants Net Flux Radiometer

S. Aslam[1,*], S. B. Calcutt[2], T. Hewagama[1], P. G. Irwin[2], C. Nixon[1], G. Quilligan[1], M. C. Roos-Serote[2], and G. Villanueva[1]

[1]*NASA Goddard Space Flight Center, Greenbelt, MD 20771, U.S.A*

[2]*Oxford University, Parks Rd., OX1 3PU, U.K*

([*]E-mail: shahid.aslam-1@nasa.gov)

Abstract: In this paper, the improved design of an Ice Giants Net Flux Radiometer (IG-NFR), for inclusion as a payload on a future Uranus probe mission, is given. IG-NFR will measure the net radiation flux, in seven spectral bands, each with a 10° Field-Of-View (FOV) and in five viewing angles as a function of altitude. Net flux measurements within spectral filter bands, ranging from solar to far-infrared, will help derive radiative heating and cooling profiles, and will significantly contribute to our understanding of the planet's atmospheric heat balance and structure, tropospheric 3-D flow, and compositions and opacities of the cloud layers. The IG-NFR uses an array of non-imaging Winston cones integrated to a matched thermopile detector Focal Plane Assembly (FPA), with individual bandpass filters and windows, housed in a vacuum micro-vessel. The FPA thermopile detector signals are read out in parallel mode, amplified and processed by a multi-channel digitizer application specific integrated circuit (MCD ASIC) under field programmable gate array (FPGA) control. The vacuum micro-vessel rotates providing chopping between FOV's of upward and downward radiation fluxes. This unique design allows for small net flux measurements in the presence of large ambient fluxes and rapidly changing temperatures during the probe descent to ≥10 bar pressure.

Keywords: Net Flux Radiometer, Ice Giants, Neptune, Uranus, Atmospheric Heat Balance.

1. Introduction

The ice giants, Uranus, and Neptune were visited for a couple of days each, in 1986 and 1989 – more than 30 years ago, from a distant Voyager 2 spacecraft fly-by, and to date never by orbiters and *in situ* probes (Hammel, 2020). They remain the last unexplored planets of our Solar System and hold vital clues to our understanding of the atmospheric dynamics and structure of planets with hydrogen atmospheres. Their atmospheres are active and complex, and storms are believed to be fueled by methane condensation, which is both extremely abundant and occurs at low optical depth [Mousis *et al*., 2018]. Given our limited knowledge of the ice giants and their large total mass contribution to shape our solar system, it is essential that we move forward on constraining their interior structure and bulk composition. Part of the effort is to comprehend more fully the transport processes by determining the global heat balance and intrinsic heat flow, thus yielding a better understanding of the interior structure and evolution of these planets. This is particularly true for Uranus for which only an upper limit on the intrinsic heat flow is known based on Voyager IRIS reflected solar radiometer data [Conrath *et al.*, 1991]. To improve model constraints on the interior structure and evolution, *in situ* probe measurements, of energy balance and interior heat flux are needed and would provide a reference profile to lift ambiguities inherent to remote observations.

Ice giant meteorology regimes depend on internal heat flux levels. Both incident solar insolation and thermal energy from the planetary interior can have altitude and location-dependent variations. Such radiative energy differences cause atmospheric heating and cooling, and result in buoyancy differences that are the primary driving force for Uranus and Neptune's atmospheric motions (Allison *et al*., 1991; Bishop *et al.*, 1995). The three-dimensional, planetary-scale circulation pattern, as well as smaller-scale storms and convection, are the primary mechanisms for energy and mass transport in the ice giant atmospheres, and are important for understanding planetary structure, circulation, and evolution (Lissauer, 2005; Dodson-Robinson *et al*., 2010; Turrini *et al*., 2014). These processes couple different vertical regions of the atmosphere and must be understood to infer properties of the deeper atmosphere and cloud decks.

The importance of understanding global heat balance and intrinsic heat flow for the ice giants was identified in the 2017 Ice Giant Pre-Decadal Study (IGPDS, 2017) report. Many authors have given compelling scientific rationale for exploration of these worlds with *in situ* probes [*e.g.*, Hofstadter *et al.*, 2019 and Mousis *et al.*, 2020]. More recently, the planetary science decadal survey released in 2022, Origins, Worlds, and Life (OWL, 2022) identified a Uranus Orbiter and Probe (UOP) as the next top priority NASA planetary flagship mission. The probe element of UOP will explore the planet's atmospheric structure and if an IG-NFR, **Fig. 1**, is included as a payload in the atmospheric structure instrument suite then it will allow for *in situ* measurements of the upward and downward radiation flux, hence net energy flux, in seven spectral channels, each with a 10° Field-Of-View (FOV) and in five sequential view angles as a function of altitude.

In this paper an IG-NFR, for inclusion as a payload on the UOP mission, is given that improves on the design reported earlier [Aslam *et al.*, 2020], ensuring more sensitive net energy flux measurements. It is important to note that although Neptune's atmospheric temperature field will be very different from that of Uranus (Hofstadter *et al.*, 2019), the only IG-NFR modification required, for operation in Neptune's atmosphere, will be a change in the bandpass filter set. IG-NFR has been designed to survive in either of the two extremely harsh atmospheric environments to ≥10 bar in pressure.

2. Instrument Modelling

2.1 Net Flux Radiometry

The basic equation relating digital count output in a given IG-NFR channel to the external radiation flux is essentially (Sromovsky *et al.*, 1992):

$$C = Kf(T/T_0)(L_u - L_d) \tag{1}$$

where K is an absolute calibration constant, $f(T/T_0)$ is a relative response function describing the instrument response dependence on detector temperature, and where L_u, L_d are the hemispherical integrals of radiance, *i.e.*, the up- and down average radiances within the detector Focal Plane Assembly (FPA) FOV respectively and are given by:

$$L_u = \int_0^\infty s_\lambda d\lambda \int_0^{\pi/2} \sin(\theta)\, d\theta \int_0^{2\pi} d\phi a_u(\theta,\phi) L(\theta,\phi,\lambda) \tag{2}$$

$$L_d = \int_0^\infty s_\lambda d\lambda \int_{\pi/2}^{\pi} \sin(\theta)\, d\theta \int_0^{2\pi} d\phi a_d(\theta,\phi) L(\theta,\phi,\lambda) \tag{3}$$

where s_λ is the relative spectral response at wavelength λ; $a(\theta, \phi)$ relative angular response at θ (angle from vertical), ϕ (azimuth angle); $L(\theta, \phi, \lambda)$, spectral radiance at wavelength λ angles θ, ϕ, where s_λ and $a(\theta, \phi)$ are both normalized to have unit integrals. Because the thermopile detectors are located in the vacuum micro-vessel, no response to external pressure is expected. Because the Winston cones have precisely defined FOVs, no crosstalk between the detectors is expected.

If we consider a flat radiation field, as an extended area blackbody, then $L(\theta, \phi, \lambda)$ is given by the Planck radiance function $B_\lambda(T)$ and eqns. (2) and (3) become:

$$L_u = \int_0^\infty s_\lambda B_\lambda(T_u) d\lambda \int_0^{\pi/2} \sin(\theta)\, d\theta \int_0^{2\pi} d\phi a_u(\theta, \phi) \tag{4}$$

$$L_d = \int_0^\infty s_\lambda B_\lambda(T_d) d\lambda \int_{\pi/2}^{\pi} \sin(\theta)\, d\theta \int_0^{2\pi} d\phi a_d(\theta, \phi) \tag{5}$$

Which reduces to the spectrally weighted average of the net Planck radiance. For a spectrally flat broadband channel, the average net radiation, L_n, is simply $L_n = (L_u - L_d)$.

Further studies are currently being carried out to understand the use of the calibration targets in this differential calculation in context of lessons learned from problems encountered in the Galileo probe net flux measurements in the Jovian atmosphere [Sromovsky *et al.*, 1998], particularly the thermal stability required between the differential measurements, as well as the implications of this differential calculation in the accuracy of the system, the findings of which will be published in the future.

2.2 Radiative Modelling

Radiative modelling of the expected IG-NFR observations, is critical to determine the optimal FOV and channel filter band selections. The modelling was done with two separate radiative transfer models: Non-linear optimal Estimator for MultivariatE spectral analySIS (NEMESIS, Irwin *et al.*, 2008) and the Planetary Spectrum Generator (PSG, Villanueva *et al.*, 2018). **Fig. 2** shows a sample calculation at a pressure level of 1 bar looking up and down at 45° to the local horizon and at an azimuth angle of 90° with respect to the Sun and shows the positions of the seven nominal filter channels. To establish the location of the filters, a sensitivity and SNR study was performed across the full spectral range and different viewing conditions (see selection of results in **Fig. 3**). Using the sensitivity study as a starting point (**Fig. 3**), and more detailed simulations for specific filter properties (as shown in **Fig. 2**), a set of filters was chosen, Table 1, that covers the bulk of the thermal emission part of the radiance field from 0.25-300 μm, and to cover varying parts of the visible-near-IR scattered solar radiation spectrum targeting several key atmospheric properties. Channel 7 is placed to capture all the scattered solar radiation, while channels 6 and 5 are placed to capture light that is progressively more absorbed by gaseous methane. Having one such methane channel would allow us some ability to differentiate between cloud opacity and methane opacity (and thus determine the abundance of both) but leaves some degeneracy due to unknown particle size. Having two such channels allows us also to make an estimate of the cloud particle size as small particles are less scattering in channel 5 than channel 6 as can clearly be seen in **Figs. 2, 3** and **4**. **Fig. 4** compares the integrated power at the detectors (for the étendue, AΩ, of the instrument with a 10° FOV) with the expected minimum detectable power of 37 pW for a 2 s integration. As can be seen, although channel 5 has the lowest integrated power of these channels, the SNR exceeds 1.0 for pressures less than 1 bar looking up and from 0.1 to 6 bar, looking down. This finding informed our decision to open the cone angle from 5° to 10°. In future work, we will examine whether the increase in SNR arising from reducing the lower wavelength of channel 5 outweighs the decrease in sensitivity to cloud particle size. Further refinement of the channel filter passbands will continue using a new web-based model, NFRViewer (Roos-Serote, 2019), which has been developed to ingest NEMESIS and PSG-calculated radiation fields and allow the user to examine the effects of selecting different NFR parameters such as the system noise performance and proposed filter boundaries.

2.3 Signal-to-Noise Ratio Performance

The IG-NFR baseline filter channels are given in **Table 1** and the predicted SNRs for these channels are given **Table 2**. The system Noise Equivalent Power (NEP) at 298 K in a 1 Hz electrical bandwidth is derived from the detector responsivity (295 V/W) divided by the summation in quadrature of all primary noise voltage sources, *i.e.,* detector Johnson noise (18 nV) and readout noise (12 nV, see Section 4.3), giving an overall system noise voltage of 22 nV, hence a system NEP of 73 pW/√Hz (*cf.* detector NEP of 60 pW/√Hz, see **Table 3**). From the Nyquist theorem, the NEP decreases inversely to the square root of the averaging time, so for a 2-s integration the minimum detectable power is 37 pW.

3. Improved IG-NFR Design

Compared to a previous IG-NFR design (Aslam *et al.*, 2020), the radiometric modelling reported here, led to the redesign of the Winston cones to capture more radiance, *i.e.*, open from 5° to 10° FOV, resulting in a much better instrument performance with higher system SNR. Opening to 10° FOV also reduced the Winston cone lengths, from ~68 mm to ~36 mm, which allowed for re-orientation of the Winston cone assembly relative to the micro-vessel window. This eliminated the need for a fold mirror and associated risks from potential reflection losses, resulting in a much smaller detector FPA and vacuum micro-vessel package, hence reducing mass, and lowering the motor power requirement. Since the divergent 10° FOV beam now looks directly out of the micro-vessel window from a close distance, this allows the use of seven smaller diameter windows to replace the single larger diameter Chemical Vapor Deposited diamond window used in the previous 5° FOV design (Aslam *et al.*, 2020). This improved design ensures that IG-NFR will survive >40 bar pressure while significantly reducing diamond window cost. The redesign allows for the FEE sub-assembly to be near the detector sub-assembly to reduce spurious noise pick-up; both assemblies are housed inside the micro-vessel, resulting in clean processed digital signals coming out of the micro-vessel, through a miniature connector, for subsequent electronic processing.

3.1 Technical Specifications

The improved IG-NFR design shown in **Fig. 1** has technical specifications as shown in **Table 4**. IG-NFR is designed to (i) accommodate seven filter bandpass channels (ii) measure up and down radiation flux in a clear unobstructed 10° FOV for all seven channels in parallel; (iii) use thermopile detectors that have a noise equivalent power of 60 pW/√Hz or better; (iv) view five distinct view angles (±80°, ±45°, and 0°); (v) understand the detector voltage responsivity as a function of focal plane temperature varying between 170-300 K; (vi) use Application Specific Integrated Circuit (ASIC) technology for the thermopile detector readout; (vii) be able to integrate radiance for 2 s or longer, and (vii) sample calibration targets every 19 s (assuming 100 m/s descent rate). Uncooled single pixel thermopile detectors are chosen for good detection sensitivity of radiation flux, **Table 3**. A close hexagonal packing arrangement of Winston cones gives seven channels, with each Winston cone designed to give a 10° clear FOV. The Winston cone non-imaging optics, detectors and filters are all housed in a micro-vessel with CVD diamond and sapphire windows. The evacuated micro-vessel mitigates rapid excursions of temperature during the probe descent, with a maximum allowed excursion of 0.5 K within one cycle of measurements within 19 s, based on an outside environment varying at 18.5 mK/s. A stepper motor with the aid of a gearbox rotates the micro-vessel, to each of the five view angles, so that the micro-vessel diamond windows have an unobstructed view through apertures in the mechanical enclosure into the atmosphere. The mechanical enclosure accommodates five apertures to view the sky in either up or down direction, a hot target, and a cold target with an embedded Light Emitting Diode (LED) for radiometric calibration, a total of 7-views (5 sky and 2 calibration) for each 19 s cycle of measurements. Nominally, the hot and cold targets are 4 K and 2 K, respectively, above the external ambient atmospheric temperature and are known within 0.1 K, further studies are ongoing to understand this thermal engineering complexity, since the external ambient temperature is changing rapidly (~25 mK/s). Since the LED is integrated into the cold target, the LED will be viewed every other cycle only between 0.1 and 0.6 bar, a full concept of operations for viewing the calibration targets has yet to be established.

3.2 System Architecture

The IG-NFR system block diagram is shown in **Fig. 5** and shows the main sub-assemblies that make up the instrument. The vacuum micro-vessel assembly houses the detector Focal Plane Assembly (FPA) integrated to the Front-End Electronics (FEE) sub-assembly where detector signals are processed and digitized by a Multi-Channel Digitizer Application Specific Integrated Circuit (MCD-ASIC). Digital signals from the MCD-ASIC are communicated out of the micro-vessel to a Field Programmable Gate Array (FPGA) housed in the Main Electronics Box (MEB) *via* a Serial Peripheral Interface (SPI). The motor drive assembly slews the micro-vessel sequentially through all the view angles, including the calibration targets.

4. Enabling Technologies

4.1 Filters and Windows

IG-NFR's seven spectral channels are defined using individual miniaturized spectral bandpass filters in combination with long and/or short wavelength blocking windows, **Table 5**.

Channel 1 uses a multi-layer coating on diamond, channels 2 and 3 are Diviner/LRO like mesh filters, channel 4 uses a multi-layer coating on CdTe, channels 5, 6 and 7 use UV-22 glass substrates in combination with short wavelength windows. The filters will be manufactured by the Infrared Multilayer Laboratory (IML) at the University of Oxford, UK. The mechanical, thermal, and optical transmission properties of substrates at 170 K have been previously reported by Hawkins, *et al.* (1998 and 2004). All channels have a field-limiting aperture in front of filter-window combination. Typical filter samples have been electron irradiated to 3 Mrad TID and cold cycled to 4 K in the past, with no degradation of transmission (Oxford private communication). The IG-NFR thermopiles are sensitive to all wavelengths that irradiate on the black absorber (low reflection), small excursions in the temperature of the filters will produce measurable signals, because the filters are sources of blackbody radiation at all wavelengths away from their narrow spectral windows. For a Noise Equivalent Thermal Difference (NETD) of 2 K, the focal plane stability requirement (of which the filters are a part of) will be between 42 mK and 740 mK depending on the instrument focal plane temperature between 170-250 K and scene temperature between 50-200 K (Foote, 1999; Sebastian *et al.*, 2009; Sebastian *et al.*, 2021; Mueller *et al.*, 2020). During the probe descent from scene temperatures 50 K to 160 K, the instrument focal plane temperature can be designed and programmed to transition gradually from 170 K to 250 K. The focal plane thermal stability requirements, including thermal gradients between system elements, are currently being analyzed and will be reported in a future publication. Temperature changes in the filters due to the changing background temperature are potentially large enough to cause a measurable, but spurious, effect. Therefore, the filter sub-assembly is mounted in good thermal contact onto a mount that is thermally coupled to the micro-vessel, ensuring the filter assembly and the micro-vessel are at the same temperature. The filter sub-assembly incorporates small aluminum alloy baffles between the filters to reduce transmission of off-axis rays produced from reflections within the micro-vessel.

4.2 MCD-ASIC

A custom radiation-hardened-by-design (RHBD) complementary metal oxide semiconductor (CMOS) MCD-ASIC, 5 mm × 5 mm die, **Fig. 6**, for operation with immunity to single event latch-up (SEL) at 123.6 MeV-cm^2/mg linear energy transfer, single event upsets (SEUs) and at least 50 Mrad total ionizing dose (TID) was designed at GSFC, using Towerjazz Semiconductor's 180 nm CMOS CA18HD process node, for high performance, near-DC signal parallel readout applications [Quilligan *et al.*, 2014, 2015, 2021; Aslam *et al.*, 2012, 2020]. The MCD-ASIC is fundamentally a readout integrated circuit (ROIC) that shares a lot of similarities with other ROICs for infrared sensor signal processing, but it also incorporates housekeeping functions to monitor the thermal and electrical environment around the ASIC. This is facilitated by a dedicated house-keeping ΣΔ analog-to-digital convertor (ADC) and programmable current sources that are used to provide thermistor, chip die temperature and other sensor measurement data. The MCD is also a rad-hard high-resolution digital voltmeter with twenty channels (variable gain up to 3125), each with a sigma-delta ADC (SD-ADC); two house-keeping channels (variable gain up to 8) sharing one SD-ADC and six transimpedance amplifiers (TIAs). A pixel channel can digitize sub-microvolt input signals while a house-keeping channel resolves inputs in the tens of microvolts. Each pixel channel has two offset and *1/f* noise reduction schemes: (1) chopper stabilization and (2) auto-zero (which adapts to any TID induced offset increases). The die is unique in that it contains twenty-one independent reference matched SD-ADCs that can broadcast digital data synchronously on twenty-one serial data lines using low voltage CMOS. Reference matching is a proprietary technique that ensures matching of the twenty-one SD-ADC transfer functions (±2%) with minimal kickback to the master reference voltages.

The MCD-ASIC is programmable with most blocks having a unique 8-bit address on an internal digital bus. An 8-bit data word defines the operating mode of a block. The digital bus is accessible via an SPI port or a parallel port. The SPI is the preferred communications port. All digital interface signals are in the range of 0 V to 1.8 V. A controller block provides all the clock signals to the chip derived from the master clock. The ASIC also includes ten 8-bit DACs, a crystal stabilized oscillator, a clock divider (tested up to 20 MHz) and a Low Voltage Differential Signal (LVDS) output pair which transmits any of the twenty channels via a digital multiplexer.

Radiation hardening was achieved with several different techniques: (1) enclosed layout transistors (ELTs) which reduce leakage in the Metal Oxide Field Effect Transistors (MOSFETs); (2) double guard-rings to prevent SEL; (3) single event upset protection (SEUP) to immunize all latches against SEUs and (4) auto-zero of amplifier offsets. SEUP forces all critical latches into a transparent state so that the chip can function with all 20 digitizer channels broadcasting data at the same gain setting.

In addition to radiation qualification, the chip was subjected to two one-week long thermal vacuum test sessions in 2018 where it continuously digitized signals from thermopile sensors. In 2014, a thermal vacuum testing session at 170 K was also successfully run. The MCD-ASIC runs off a 1.8 V nominal supply voltage drawing a maximum of 200 mA when all channels are operating at the full data rate (3 MHz). The entire ROIC can be put into standby mode drawing a few tens of microamps of current or individual channels can be powered down. It is a versatile system on a chip (SoC) with differential signal processing from the front-end through to the ΣΔ ADCs.

The ASIC will reside on a FEE readout board providing 1.8 V derived from 3.3 V power supply. The interface to the MEB will be via SPI protocol. Other than 3.3 V and ground, no analog signals will be transmitted to or from the MEB. The MEB provides a clock reference while the MCD sends back digital data related to the thermopile outputs and thermistor temperature readings.

4.3 FEE Sub-Assembly

The FEE sub-assembly has been demonstrated, i.e., (i) FPGA control of the MCD-ASIC through SPI protocol; (ii) the ΣΔ modulator with a digital Sinc filter to remove the high frequency noise and decimate the single bit stream to a high-resolution data word (iii) the convolution of the ΣΔ ADC frequency response and the filter resulting in a dramatic reduction in the *1/f* noise of the amplified signal is shown in **Fig. 7**; (iv) in-house firmware for the FPGA to verify the operation of the MCD-ASIC. A third order Sinc filter was employed on the FPGA to decimate the single bit stream into 24-bit data words with a modulation frequency of 250 kHz and over sampling rate of 1024; (v) the readout noise under FPGA control of the system is shown in **Fig. 8** and (vi) operation of the parallel readout circuit using an infrared broadband source and filter bands centered at 2.7 μm, 4.26 μm and 3.95 μm is shown in **Fig. 9** **[**Tran *et al.,* 2020**]**.

4.4 MEB Electronics

The MEB assembly, **Fig. 10,** consists of five CubeSat-sized cards: the SpaceCube Mini-Z card, a Low Voltage Power Converter (LVPC) card, a Power Switching Input Output (I/O) card, a Motor Drive Control (MDC) card, and a passive backplane card that interfaces the system together. These designs emphasize a hybrid architecture, combining radiation-hardened and commercial components with years of space design experience [Brewer, *et al.,* 2020; George, *et al.,* 2018; Petrick, *et al.,* 2015; Fabula, *et al.,* 2008].

The primary prototype computer is the SpaceCube Mini-Z, a hybrid space computer featuring the Xilinx Zynq SoC (28 nm FPGA). The main processing element is the Xilinx Zynq-7020 SoC (dual ARM Cortex-A9/NEON cores and reconfigurable Artix-7 FPGA fabric). There are connections from the FPGA and ARM side of the Zynq that can be configured in a combination of varying communication interfaces including UART, I2C, SPI, as well as general-purpose IO. The Mini-Z supports up to 1 GB of DDR3 memory, and 4 GB of non-volatile, radiation-tolerant, Not AND (NAND) Flash memory from 3D-Plus for mission storage to capture all science data, spacecraft housekeeping data, and finally multiple copies of the flight software code. The SpaceCube Mini-Z is equipped with a prebuilt, thoroughly tested software package for Core Flight System (cFS), NASA Goddard's open-source, reusable, flight-software framework.

The LVPC card has been designed for the CODEX mission on the space station and relies on thoroughly tested design practices used for similar cards. This design is an evolution of two heritage LVPC designs used on Space Test Program – Houston 6 (STP-H6) and the SpaceCube v2.0 Mini on STP-H5. The LVPC includes all radiation-hardened regulators and provides the system with voltage regulators to power the LEDs, Motor, and SpaceCube Mini-Z.

The power switching, I/O card is designed to interface the connectors with the MCD-ASIC and control power to the heaters. This design also encapsulates ADCs needed to perform health and status monitoring of the instrument.

The MDC card includes several H-bridge circuits and uses PWM to control the MDC card. The backplane card is passive and is the interconnect between the card slots.

4.5 Light Emitting Diode

The proposed, on-site and in-situ, calibration LED, as indicated in Section 3.1 and shown in **Fig. 11**, will be selected from one of the Sensor Electronic Technology, Incorporated. These LEDs are fabricated from AlGaN semiconductor, a material that is inherently radiation hard due to its wide electronic band gap [Aslam *et al.*, 2005]. Three types of LED's have been tested for displacement dose, *i.e.*, TUD69H1B (260-270 nm spectral emission), TUB89H1B (280-290 nm spectral emission), and TCE49H1B (310 nm spectral emission). A detailed trade study will be conducted in order to pick the optimal wavelength LED for the NFR calibration needs. All three LEDs use the same diode material stoichiometry but with different hemispherical cover glass transmissive windows to obtain different wavelength emissions.

Radiation testing was carried out at Crocker Nuclear Laboratory, on the campus of The University of California at Davis, by exposing the devices to 64 MeV protons at a fluence of 1E5 p^+/cm^2. Four TUD69H1Bs, four TUD89H1Bs, and seven TEC49H1Bs were irradiated, and one of each type was used as a control. Prior to the first radiation dose, all parts were electrically tested. After each exposure level, the parts (including the controls) were tested again. Devices were subjected to multiple levels of displacement damage dose between 0 and 300 krad (Si) TID dose. Specification thresholds were set in accordance with the LEDs' datasheets. The forward current-voltage sweep was conducted in 10 mV steps at each dose steps. Changes in the voltage with forward current set at 20 mA was recorded. The maximum forward voltage was 7 V at the forward current of 20 mA. All LED's survived at 300 krad (Si) TID with all electrical and optical parameters remaining in specification to those listed in the manufacturers LED datasheets [Casey, 2017]. One LED (TEC49H1B) was taken to 3.5 Mrad (Si) at the same proton fluence and showed darkening of glass window and passed liveliness testing.

5. Data Volume

The notional IG-NFR operational scenario as the probe descends deep into the atmosphere of Uranus is given in **Fig. 11.** The probe descent sequence has been taken from the IGPDS study report. **Table 6** shows the science and housekeeping data collection for a 90-minute descent from 0.1 to 10 bar, the total mission science data volume is ~0.6 Mb.

6. Conclusions

The 2022 OWL planetary decadal report recommended the Uranus Orbiter and Probe as the next highest priority flagship mission for NASA. An understanding of planetary atmospheric circulation structure in the Uranus system requires knowledge of the vertical profile of radiative heating and cooling and its horizontal distribution. *In situ* measurements with the IG-NFR described here, as part of an atmospheric instrument suite, on a probe descending deep into the atmosphere, will determine the balance between the upward and downward solar and thermal radiation fluxes. These measurements will help unravel the mystery of why Uranus's upper limit of intrinsic heat flow, determined by Voyager 2 radiometric data, is three times lower than that of Neptune's value, *i.e.*, about three times higher than the chondritic value. Determination of the actual Uranus heat flow value rather than an upper limit would greatly constrain interior structure *via* thermal history models and clarify the difference in heat flow as compared with Saturn and Neptune.

The IG-NFR will also provide complementary data to science instruments measuring visible albedo and thermal emission at a range of solar phase angles and incidence angles from the orbiter. These measurements will provide ground truth for radiative transfer models of remote sensing data.

Funding

We thank NASA Goddard Space Flight Center for research and development funds, and the NASA ROSES PICASSO program (*NNH17ZDA001N-PICASSO*) for supporting the design and technology maturation of the IG-NFR.

Disclosures

The authors declare that they have no known competing financial interests or personal relationships that could have appeared to influence the work reported in this paper.

Acknowledgement

Special thanks to Mr. William A. Mamakos, from Design Interface Inc., Finksburg, MD, USA, for providing expertise in mechanical computer aided design, Dr. C. M. Wilson for expertise on SpaceCube electronics, and Mr. Dat Tran, a PhD candidate, at Catholic University of America, Washington DC, USA, for assembling and testing front-end readout electronics for thermopile detectors.

Author ORCID ID’s

Shahid Aslam: 0000-0001-9581-647X

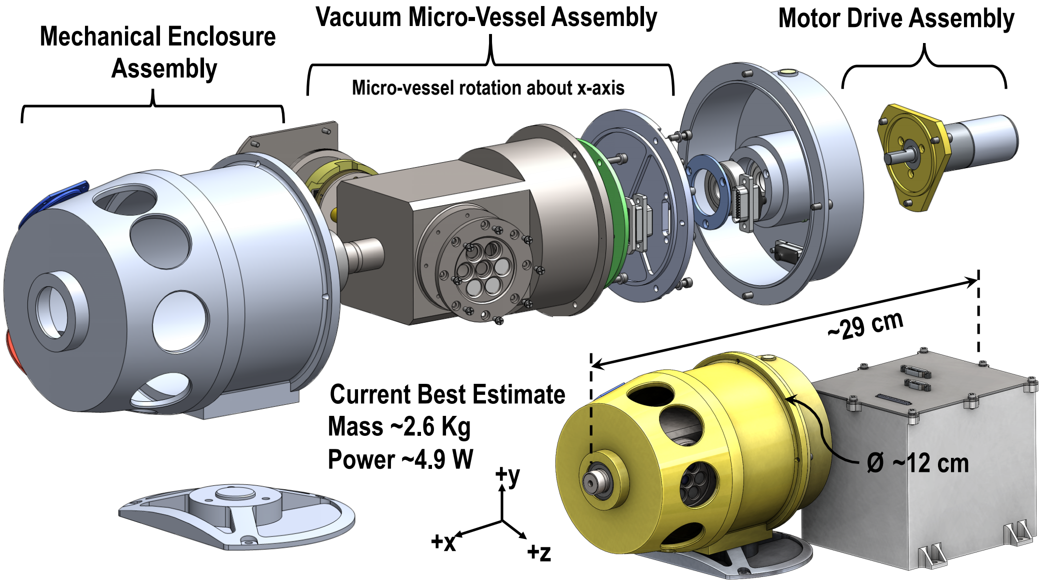

Fig. 1. *Top:* Exploded view of IG-NFR showing the vacuum micro-vessel, motor drive and mechanical enclosure assemblies. *Bottom:* Shows the assembled IG-NFR and the main electronics box with nominal dimensions. The improved IG-NFR design is capable of measuring energy flux in seven spectral channels from 0.2-300 µm in spectral wavelength, each with a 10° FOV projected into the sky, in five viewing angles. The rapidly changing temperature environment at Uranus during probe descent, from ~50 K (~0.1 bar) to ~160 K (~10 bar), is mitigated using a vacuum micro-vessel.

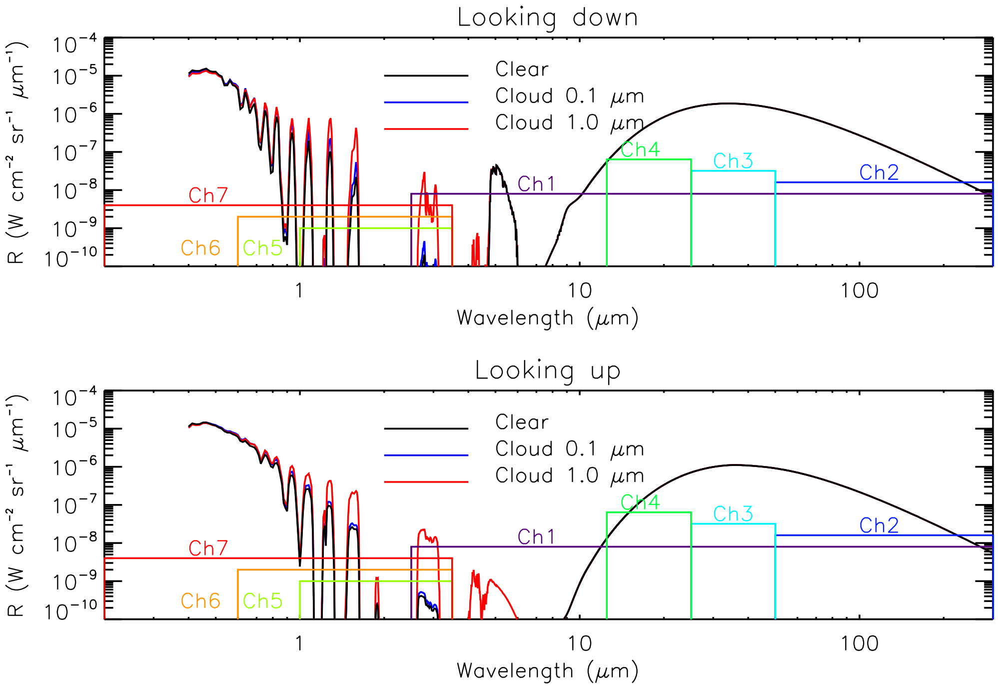

Fig. 2. Synthetic NEMESIS calculation of the radiance field seen by IG-NFR at a pressure level of 1 bar in Uranus's atmosphere and 45° above the horizon and 90° azimuth with respect to the Sun. The radiances are calculated for three cases: 1) assuming our nominal cloud model with 1.0 µm particles; 2) for cloud-free conditions; and 3) for the case where the cloud particle size has been reduced to 0.1 µm.

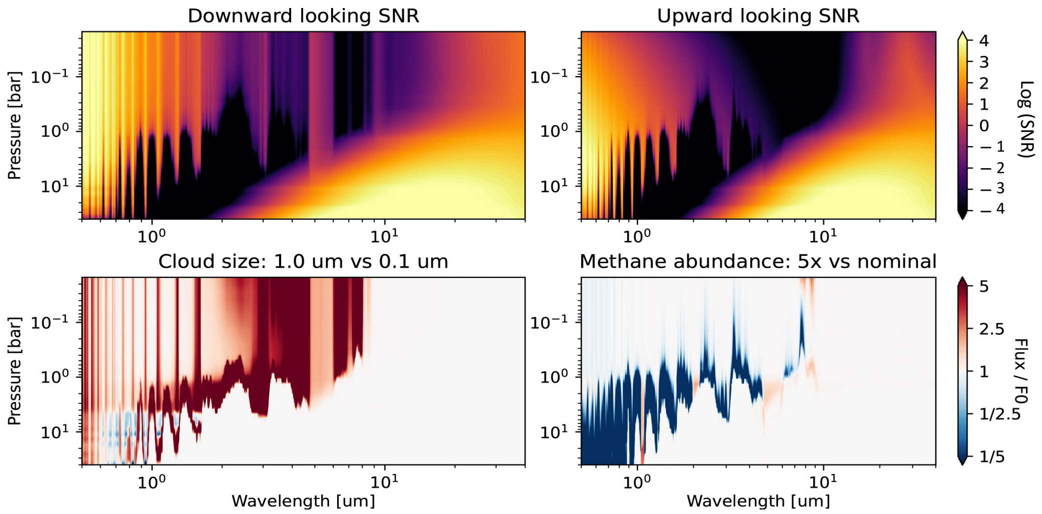

Fig. 3. Synthetic PSG calculations presenting SNR for downward and upward looking geometries and sensitivity studies to particle size and methane abundance. The simulations are done considering a 10° FOV, a solar zenith angle of 0°, emission angle of 45°, an integration time of 2-seconds, and a filter width of 1 µm.

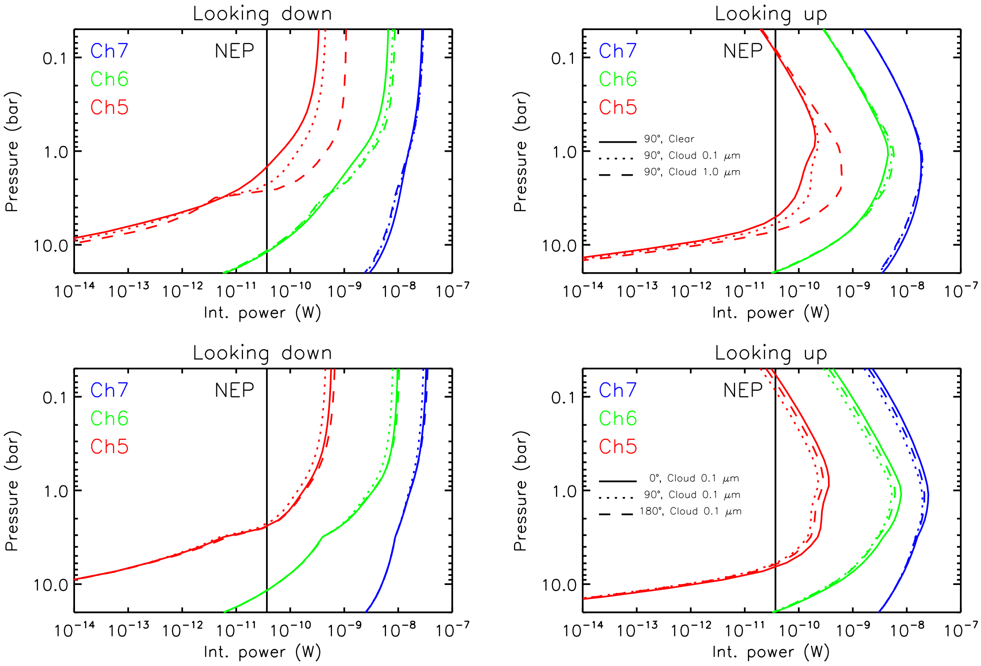

Fig. 4. Synthetic NEMESIS calculations (upwards and downwards at ±45° zenith angle) of the integrated power gathered by IG-NFR in channels 5, 6 and 7 as a function of pressure level for different conditions. In the top row we show the calculations at an azimuth angle of 90° and three different cloud cases: 1) clear, *i.e.*, no clouds; 2) nominal cloud model with 1.0 µm radius particles; and 3) nominal cloud model with particle radius reduced to 0.1 µm. In the bottom row, we show our calculations for the cloud model with particle radius of 0.1 µm, and three different azimuth angles (0° – forward scattering, 90°, and 180° – back-scattering) Also plotted in all panels is the expected minimum detectable power of 37 pW for a 2-s integration. The variation with azimuth angle can be seen to be significant and hence as the probe descends and rotates, this angle will need to be reconstructed from the dataset in order to then use these data to determine the vertical distribution and size of the cloud particles.

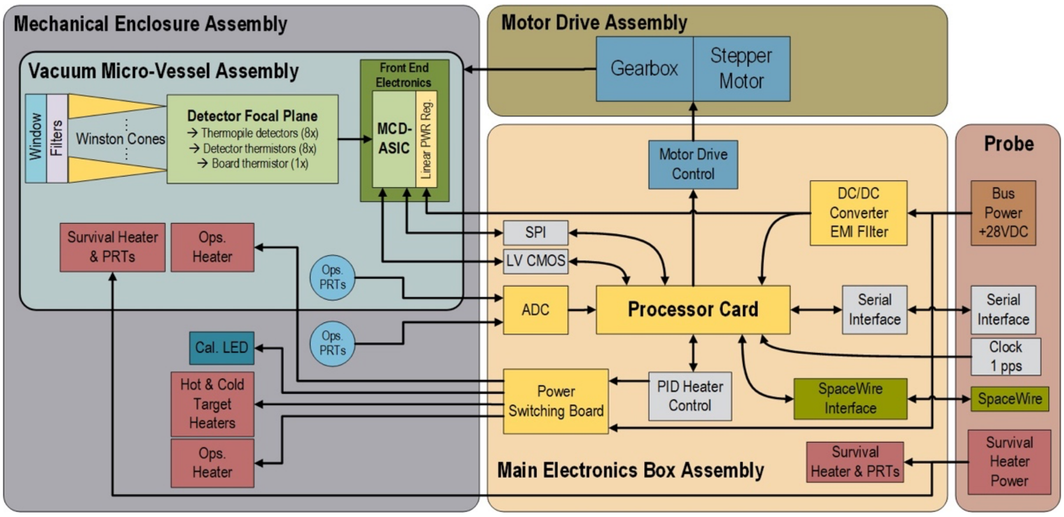

Fig. 5. IG-NFR system block diagram.

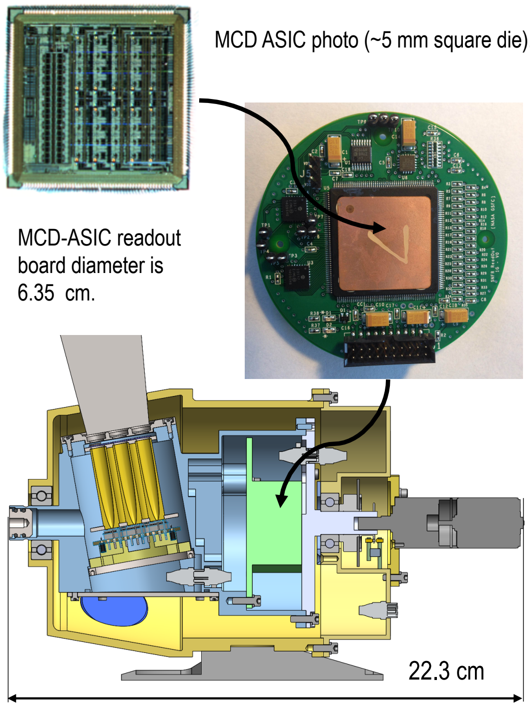

Fig. 6. MCD-ASIC readout board is housed inside a vacuum micro-vessel and near to the detector sub-assembly.

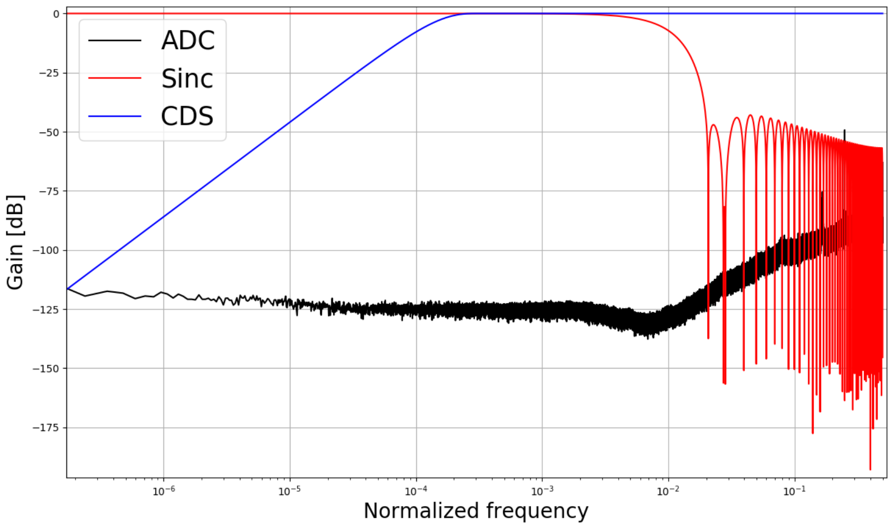

Fig. 7. Frequency response of the parallel readout system. Note that the correlated double sampling response only applies to the noise signal. (ADC – Analog-to-Digital Convertor; Sinc - third order Sinc filter; CDS – Correlated Double Sampling).

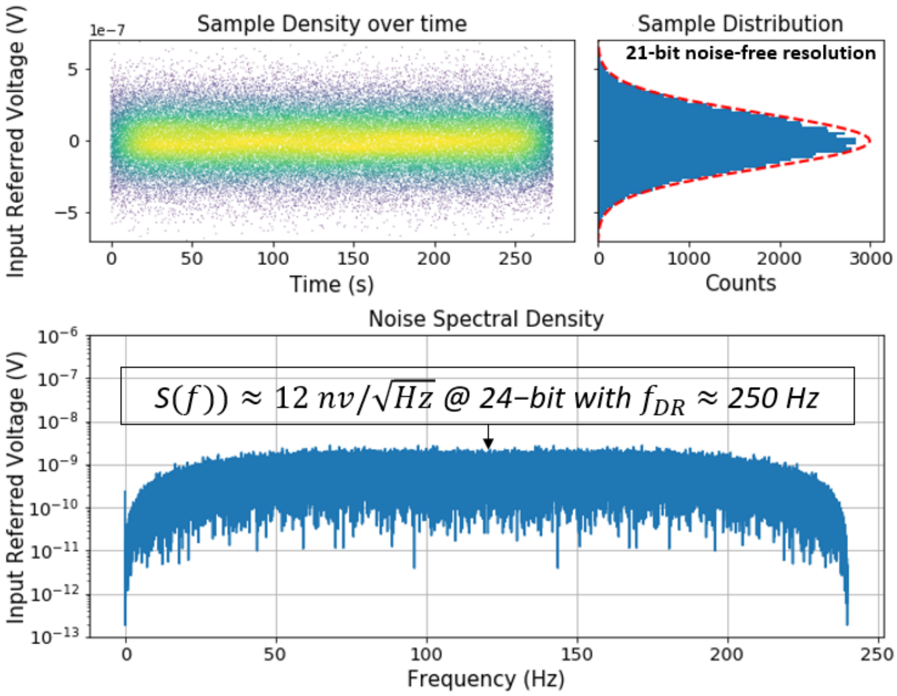

Fig. 8. MCD-ASIC noise spectrum with output data rate at 250 Hz, channel gain of 250, and modulating frequency of 64 kHz. A low readout noise performance of ~12 nV/√Hz is shown in the low frequency region [Aslam, *et al*., 2020].

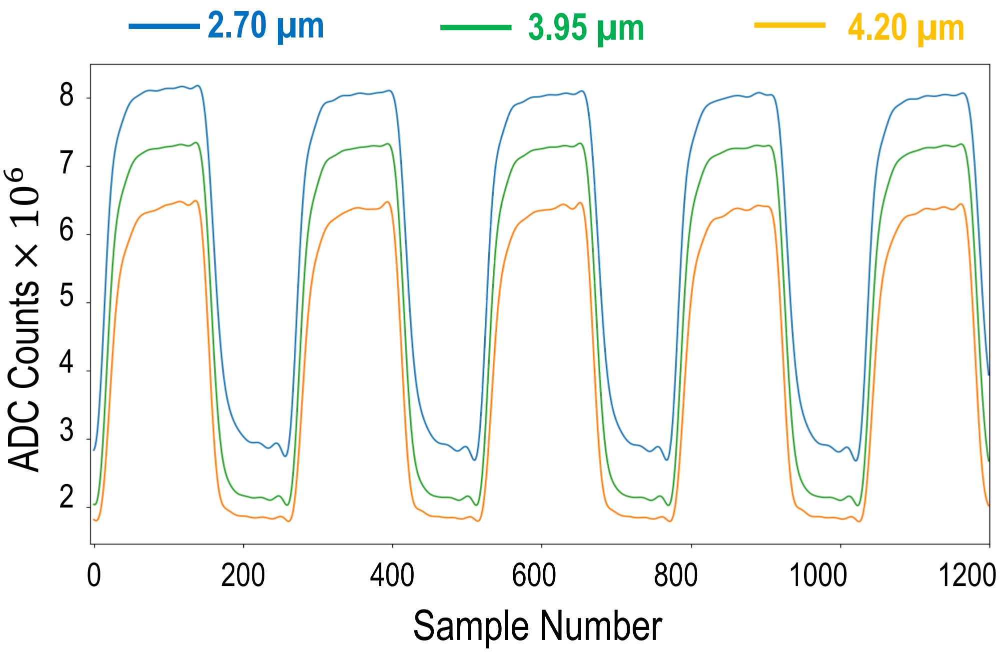

Fig. 9. To check the parallel readout circuit ADC response, we chose three narrow band spectral channels, centered at 2.7 µm, 3.95 µm, and 4.2 µm wavelength, that were readily available in the laboratory. An infrared source is pulsed at 1 Hz which takes 250 samples to finish a cycle at output data rate of 250 Hz.

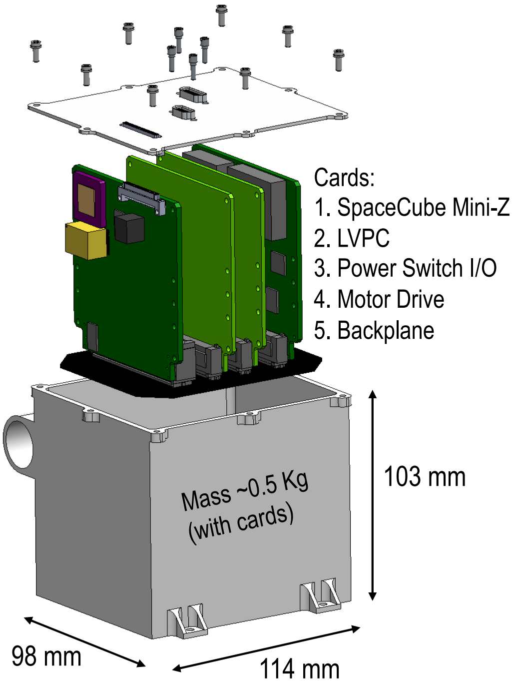

Fig. 10. MEB assembly showing five CubeSat-sized cards including backplane.

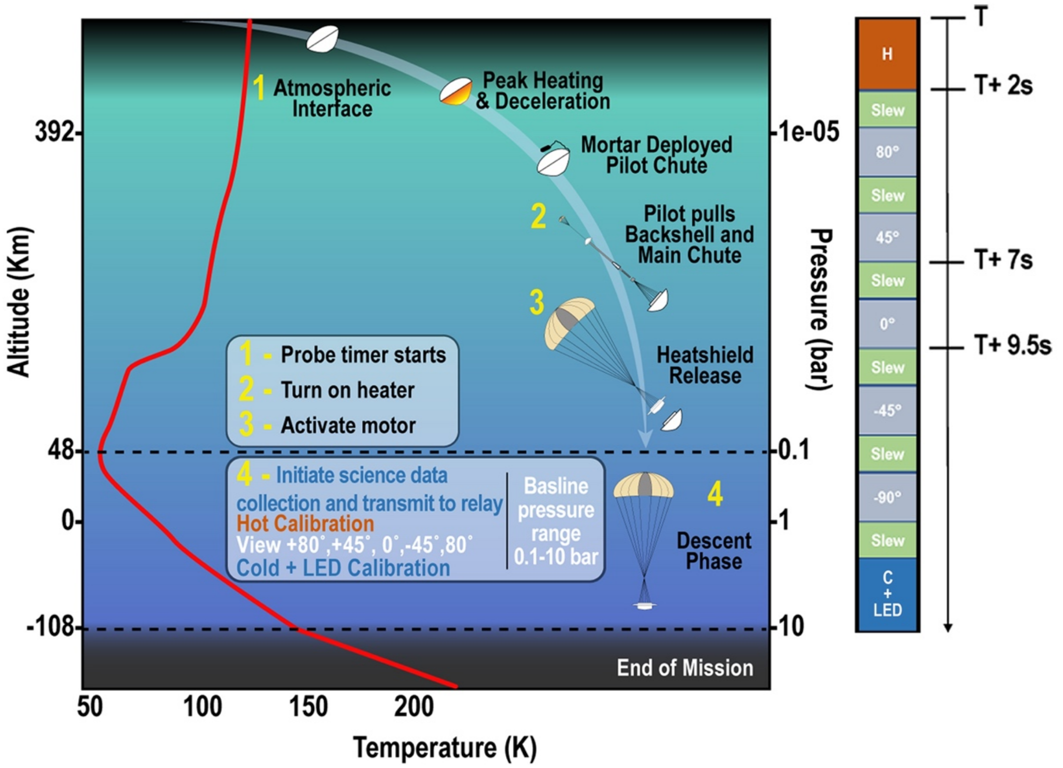

Fig. 11. IG-NFR operation during a probe descent from 0.1 to 10 bar. The LED will be used between 0.1 and 0.6 mbar, the exact sequencing of hot/cold/LED target views has yet to be defined through a rigorous Con-Ops analysis. The timing sequence for IG-NFR sky view angles and calibration targets is also shown to the right. The science, housekeeping and auxiliary data volume for a 90-minute mission is ~0.6 MB, based on a 2 second integration at each viewing angle including calibration targets and a descent rate of ~30 m/s.

Table 1. Baseline IG-NFR bandpass filter channels and measurement objectives, determined through radiative modelling, to maximize science return from Uranus's atmosphere.

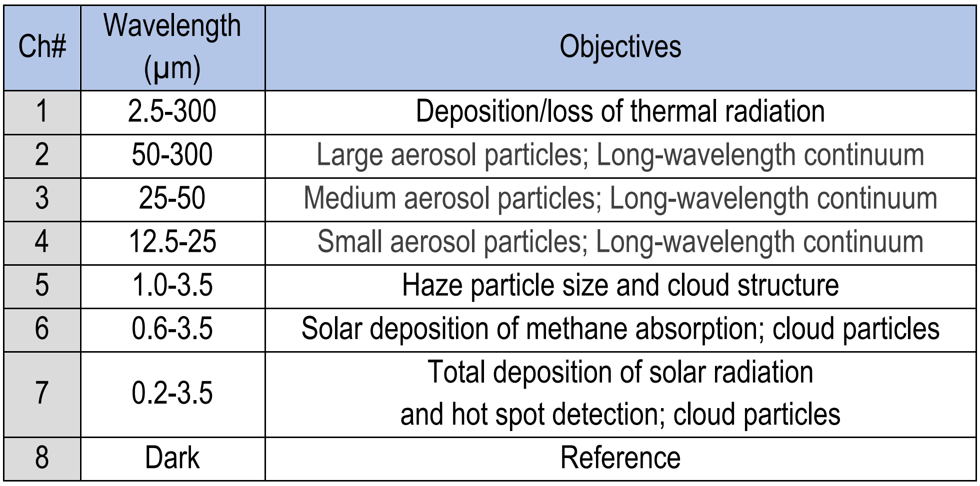

Ch#	Wavelength (µm)	Objectives
1	2.5-300	Deposition/loss of thermal radiation
2	50-300	Large aerosol particles; Long-wavelength continuum
3	25-50	Medium aerosol particles; Long-wavelength continuum
4	12.5-25	Small aerosol particles; Long-wavelength continuum
5	1.0-3.5	Haze particle size and cloud structure
6	0.6-3.5	Solar deposition of methane absorption; cloud particles
7	0.2-3.5	Total deposition of solar radiation and hot spot detection; cloud particles
8	Dark	Reference

Table 2. SNR's calculated using NEMESIS. Simulation assumes a cloud structure with a solar elevation angle of 10° (above horizon), emission (viewing) angle of 45°, FOV of 10° and an integration time of 2 s.

Ch #	Filter (μm)	0.1 bar		1 bar		10 bar	
		up	down	up	down	up	down
1	2.5-300	3092	243	10908	10532	293820	293820
2	50-300	2296	181	5920	5720	33896	33896
3	25-50	763	57	4421	4244	98695	98695
4	12.5-25	11	5	609	609	132198	132198
5	1.0-3.5	30	9	14	21	N/A	N/A
6	0.6-3.5	196	34	61	164	N/A	N/A
7	0.2-3.5	560	125	165	463	N/A	N/A

Table 3. Thermopile detector parameters. Thermopiles with custom gold black absorbers have a >90% absorption from 0.2 to 300 μm.

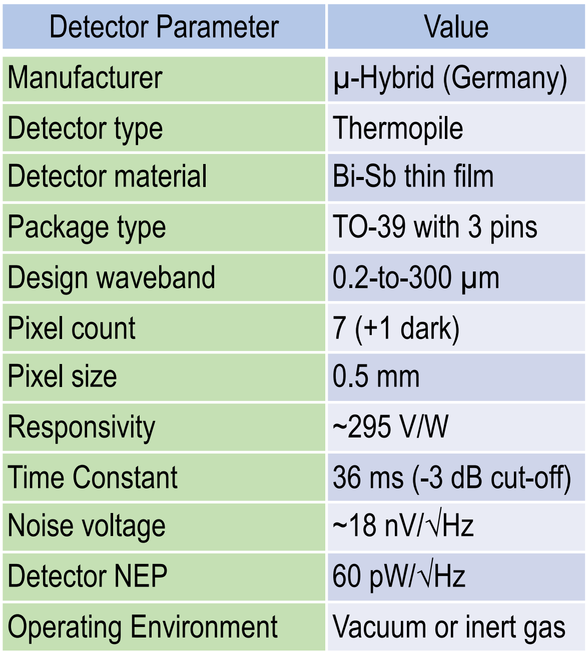

Detector Parameter	Value
Manufacturer	μ-Hybrid (Germany)
Detector type	Thermopile
Detector material	Bi-Sb thin film
Package type	TO-39 with 3 pins
Design waveband	0.2-to-300 μm
Pixel count	7 (+1 dark)
Pixel size	0.5 mm
Responsivity	~295 V/W
Time Constant	36 ms (-3 dB cut-off)
Noise voltage	~18 nV/√Hz
Detector NEP	60 pW/√Hz
Operating Environment	Vacuum or inert gas

Table 4. IG-NFR technical specifications designed to meet the science objectives for net energy flux measurements in the atmospheres of the ice-giants.

Parameter	IG-NFR
Spectral range	0.2 to 300 μm
Optics	Non-imaging Winston cones
Channels	7 science + 1 dark
Field-Of-View	10 degrees
Viewing angles	±80°; ±45° and 0° relative to nadir/zenith
Detectors (uncooled)	7 thermopile pixels + 1 dark
Pixel size	0.5 mm diameter
Basic Mass	~ 2.6 kg
Basic power	~ 4.9 W
Volume (w/o MEB)	~552 cm^3
Data volume (90 mins)	580 kbits
Operating modes	36 ms integration
Observation strategy	Sequential rotation into five sky view angles

Table 5. IG-NFR filter channel materials.

Ch#	Filter Bandwidth (µm)	Filter Type (IML, Oxford)
1	2.5-300	Multi-layer coating on diamond
2	50-300	Diviner-like mesh
3	25-50	Diviner-like mesh
4	12.5-25	CdTe substrate
5	1.0-3.5	UV22 plus Si
6	0.6-3.5	UV22 plus Schott glass
7	0.2-3.5	UV22

Table 6. IG-NFR data volume.

Data	Name	Bit #	Sample #	Total bits	Sampling Interval (s)	Volume (Mb)
Thermal	Fan-out board Temperature	12	1	12	7.5	0.00864
	Vessel Temperature	12	1	12	7.5	0.00864
	Windows Temperature	12	1	12	7.5	0.00864
Science	Thermopile Data	24	8	192	2.5	0.41472
	Thermistor on thermopile can	16	8	128	7.5	0.09216
Auxilary	Hot Target Temperature	12	1	12	7.5	0.00864
	Cold Target Temperature	12	1	12	7.5	0.00864
	LED status	1	1	1	7.5	0.00072
	Motor Position	3	1	3	2.5	0.00648
	Survival Heater Status	1	1	1	7.5	0.00072
	Time Stamp	11	1	11	2.5	0.02376
Total						0.58176

References

Allison, M., Beebe, R. F., Conrath, B. J., Hinson, D. P., Ingersoll, A. P. 1991. Uranus atmospheric dynamics and circulation. Uranus p. 253-295.

Aslam, S., Yan, F., Pugel, D. E., Franz, D., Miko, L., Herrero, F., Matsumara, M., Babu, S., Stahle, C. M. 2005. "Development of ultra-high sensitivity wide-band gap UV-EUV detectors at NASA Goddard Space Flight Center," Proc. SPIE 5901, Solar Physics and Space Weather Instrumentation, 59011J (18 August 2005); doi: 10.1117/12.639415

Aslam, S., Akturk, A., Quilligan, G. 2012. A Radiation Hard Multi-Channel Digitizer ASIC for Operation in the Harsh Jovian Environment, In Extreme Environment Electronics, Ed. J. D. Cressler, H. A. Mantooth, CRC Press, Boca Raton, FL, Nov. 2012, ISBN: 978-1-4398-7430-1.

Aslam, S., Achterberg, R. K., Calcutt, S. B., *et al.* 2020. “Advanced Net Flux Radiometer for the Ice Giants,” Space Sci. Rev. 216:11

Bishop, J., Atreya S. K., Romani P. N., Orton G. S., Sandel B. R., Yelle, R. V. 1995. Book Chapter in Neptune and Triton by D. P. Cruikshank, Mildred Shapley Matthews, A. M.

Brewer, C., Franconi, N., Ripley, R., Geist, A., Wise, T., Sabogal, S., Crum, G., Heyward, S., and Wilson, C. 2020. “NASA SpaceCube Intelligent Multi-Purpose System for Enabling Remote Sensing, Communication, and Navigation in Mission Architectures,” 34th Annual AIAA/USU Conf. on Small Satellites, SSC20-VI-07, Logan, UT, Aug. 1-6, 2020.

Casey, M., Phan, A., UV LED Displacement Damage Dose Test Report. 2017. GSFC Internal Private Communication.

Dodson-Robinson, S. E., Bodenheimer, P. 2010. The formation of Uranus and Neptune in solid-rich feeding zones: Connecting chemistry and dynamics. Icarus 207, 491-498.

Fabula, J. J., DeJong, J. L., Lesea, A., and Hsieh, W. 2008. The total ionizing dose performance of deep sub-micron CMOS processes. In Proc. of Military and Aerospace Programmable Logic Devices Conference (MAPLD’08). Annapolis, MD. https://nepp.nasa.gov/mapld_2008/presentations/w/08-Fabula_Joseph_mapld08 _pres_2.pdf.

Foote, M.C. 1999. "Temperature stabilization requirements for unchopped thermal detectors," Proc. SPIE 3698, Infrared Technology and Applications XXV, (26 July 1999); doi: 10.1117/12.354536

George A.D., and Wilson, C.M. 2018. "Onboard Processing with Hybrid and Reconfigurable Computing on Small Satellites," in Proceedings of the IEEE, vol. 106, no. 3, pp. 458-470, March 2018, doi: 10.1109/JPROC.2018.2802438.

Hammel, H. B., (2020), Lessons Learned from (and since) Voyager 2 flybys of Uranus and Neptune, Phil. Trans. R. Soc. A. doi:10.1098/not yet assigned.

Hawkins, G. J., Hunneman, R., Gardner, M.T., Babcock, G.T. 1998. “An ultra-wide passband (5–30 μm) filter for FTIR studies of Photosystem II,” Infrared Physics & Technology, Volume 39, Issue 5, 1998, Pages 297-306, ISSN 1350-4495, https://doi.org/10.1016/S1350-4495(98)00021-8.

Hawkins, G., Hunneman, R. 2004. “The temperature-dependent spectral properties of filter substrate materials in the far-infrared (6–40 μm),” Infrared Physics & Technology, Volume 45, Issue 1, 2004, Pages 69-79, ISSN 1350-4495, https://doi.org/10.1016/S1350-4495(03)00180-4.

Hofstadter, M., Simon, A., Atreya, S., Banfield, D., Fortney, J. J., Hayes, A., Hedman, M., Hospodarsky. G., Mandt, K., Masters, A., Showalter, M., Soderland, K. M., Turrini, D., Turtle, E., Reh, K., Elliot, J., Arora, N., Petropoulos, A., The Ice Giant Study Team. 2019. Uranus and Neptune missions: A study in advance of the next Planetary Science Decadal Survey. Planetary and Space Science, 177, 104680.

Ice Giants Pre-Decadal Survey Mission Study (IGPDS 2017) Report (JPLD-100520), https://www.lpi.usra.edu/icegiants/mission_study/

Irwin, P. G. J., Teanby, N. A., de Kok, R., Fletcher, L. N., Howett, C. J. A., Tsang, C. C. C., Wilson, C. F., Calcutt, S. B., Nixon, C. A., and Parrish, P. D. (2008). The NEMESIS planetary atmosphere radiative transfer and retrieval tool. *Journal of Quantitative Spectroscopy and Radiative Transfer*, **109**:1136–1150, April 2008. doi: 10.1016/j.jqsrt.2007.11.006.

Lissauer, J. J. 2005. Formation of the Outer Planets. Space Science Reviews 116, 11-24.

Mousis, O.J., Atkinson, Cavalié, T., *et al*. 2018. “Scientific rationale for Uranus and Neptune in situ explorations,” Planetary and Space Science 155 (2018) 12–40, https://doi.org/10.1016/j.pss.2017.10.005

Mueller, N. T., Knollenberg, J., Grott, M., Kopp, E., Walter, I., Krause, C., *et al*. 2020. Calibration of the HP3 radiometer on InSight. Earth and Space Science,7, e2020EA001086. https://doi.org/10.1029/2020EA001086

OWL 2022, National Academies of Sciences, Engineering, and Medicine, Origins, Worlds, and Life: A Decadal Strategy for Planetary Science and Astrobiology 2023-2032 (National Academies Press, 2022).

Petrick, D., Gill, N., Hassouneh, M., Stone, R., Winternitz, L., Thomas, L., Davis, M., Sparacino, P., and Flatley, T. 2015. “Adapting the SpaceCube v2.0 data processing system for mission-unique application requirements,” IEEE Aerospace Conference, Big Sky, MT, June 15-18, 2015.

Quilligan, G., Aslam, S., Lakew, B., DuMonthier, J., Katz, R., and Kleyner, I. 2014. A 0.18μm CMOS Thermopile Readout ASIC Immune to 50 Mrad Total Ionizing Dose (Si) and Single Event Latchup to 174 MeV-cm^2/mg. International

Workshop on Instrumentation for Planetary Missions (IPM- 2014), November 2014, Greenbelt, MD 20771.

Quilligan, G., DuMonthier, J., Aslam, S., Lakew, B., Kleyner, I., Katz, R. 2015. Thermal Radiometer Signal Processing using Radiation Hard CMOS Application Specific Integrated Circuits for use in Harsh Planetary Environments. European Planetary Science Congress 2015 held 27 September - 2 October 2015 in Nantes, France.

Quilligan, G., and Aslam, S. 2021. TID and Heavy Ion Performance of a RHBD Multi-Channel Digitizer in 180 nm CMOS IEEE Transactions on Nuclear Science 68 (7) July 2021: 1414-1422 [10.1109/tns.2021.3080179]

Roos-Serote, M. C. 2019. Private Communication *via* e-mail (27th November 2019).

Sebastián, E., Armiens, C., Gómez-Elvira, J. 2011. “Infrared temperature measurement uncertainty for unchopped thermopile in presence of case thermal gradients.” Infrared Physics & Technology, Volume 54, Issue 2, 2011, Pages 75-83, ISSN 1350-4495, https://doi.org/10.1016/j.infrared.2010.12.038.

Sebastián, E., Martínez, G., Ramos, M., Pérez-Grande, I., Sobrado, J., J. A. Rodríguez Manfredi. 2021. “Thermal calibration of the MEDA-TIRS radiometer onboard NASA's Perseverance rover.” Acta Astronautica, Volume 182, 2021, Pages 144-159, ISSN 0094-5765, https://doi.org/10.1016/j.actaastro.2021.02.006.

Sromovsky, L. A., Best, F. A., Revercomb, H. E., Hayden, J. 1992. “Galileo Net Flux Radiometer Experiment.” *Space Sci Rev* **60**, 233-262.

Sromovsky, L. A., Collard, A. D., Fry, P. M., Orton, G. S., Lemmon, M. T., Tomasko, M. G., and Freedman, R. S. 1998. “Galileo probe measurements of thermal and solar radiation fluxes in the Jovian atmosphere.” Journal of Geophysical Research, Vol. 103, No. E10. pages 22,929-22,977.

Tran, D., Gorius, N., Aslam, S., Glavin, D. P., *et al*. 2020. "Radiation-hard parallel readout circuit for low-frequency voltage signal measurements." *Sensors and Systems for Space Applications XIII*, **11422 (1142205).**

Turrini, D., and 14 colleagues 2014. The comparative exploration of the ice giant planets with twin spacecraft: Unveiling the history of our Solar System, Planetary and Space Science 104, 93-107.

Villanueva, G. L., Smith, M. D., Protopapa, S., Faggi, S., & Mandell, A. M. 2018. “Planetary Spectrum Generator: An accurate online radiative transfer suite for atmospheres, comets, small bodies and exoplanets,” Journal of Quantitative Spectroscopy and Radiative Transfer, ISSN: 0022-4073, Vol: 217, Page: 86-104, 2018; doi:10.1016/j.jqsrt.2018.05.023